AGU PUBLICATIONS

JGR

Journal of Geophysical Research: Earth Surface

RESEARCH ARTICLE

10.1002/2016JF004072

Key Points:
- Flow separation/reattachment has a significant effect on fluid turbulent structures and the pattern of sediment transport downstream
- Immediately downstream of flow reattachment, sediment transport is dominated by localized, intermittent, multidirectional transport events
- Localized, intermittent, multidirectional transport events are a result of discrete, 3-D turbulent events reported here as splat events

Supporting Information:
- Supporting Information S1
- Figure S1
- Figure S2
- Figure S3
- Figure S4
- Figure S5
- Figure S6
- Figure S7

Correspondence to:
K. C. P. Leary,
learykcp@asu.edu

Citation:
Leary, K. C. P., & Schmeeckle, M. W. (2017). The importance of splat events to the spatiotemporal structure of near-bed fluid velocity and bed load motion over bed forms: Laboratory experiments downstream of a backward facing step. *Journal of Geophysical Research: Earth Surface*, *122*, 2411–2430. https://doi.org/10.1002/2016JF004072

Received 31 AUG 2016
Accepted 6 NOV 2017
Accepted article online 15 NOV 2017
Published online 22 DEC 2017

The Importance of Splat Events to the Spatiotemporal Structure of Near-Bed Fluid Velocity and Bed Load Motion Over Bed Forms: Laboratory Experiments Downstream of a Backward Facing Step

K. C. P. Leary[1] **and M. W. Schmeeckle**[2]

[1] School of Earth and Space Exploration, Arizona State University, Tempe, AZ, USA, [2] School of Geographical Sciences and Urban Planning, Arizona State University, Tempe, AZ, USA

Abstract Flow separation/reattachment on the lee side of alluvial bed forms is known to produce a complex turbulence field, but the spatiotemporal details of the associated patterns of bed load sediment transported remain largely unknown. Here we report turbulence-resolving, simultaneous measurements of bed load motion and near-bed fluid velocity downstream of a backward facing step in a laboratory flume. Two synchronized high-speed video cameras simultaneously observed bed load motion and the motion of neutrally buoyant particles in a laser light sheet 6 mm above the bed at 250 frames/s downstream of a 3.8 cm backward facing step. Particle Imaging Velocimetry (PIV) and Acoustic Doppler Velocimetry (ADV) were used to characterize fluid turbulent patterns, while manual particle tracking techniques were used to characterize bed load transport. Octant analysis, conducted using ADV data, coupled with Markovian sequence probability analysis highlights differences in the flow near reattachment versus farther downstream. Near reattachment, three distinct flow patterns are apparent. Farther downstream we see the development of a dominant flow sequence. Localized, intermittent, high-magnitude transport events are more apparent near flow reattachment. These events are composed of streamwise and cross-stream fluxes of comparable magnitudes. Transport pattern and fluid velocity data are consistent with the existence of permeable "splat events," wherein a volume of fluid moves toward and impinges on the bed (sweep) causing a radial movement of fluid in all directions around the point of impingement (outward interaction). This is congruent with flow patterns, identified with octant analysis, proximal to flow reattachment.

1. Introduction

In low-gradient alluvial rivers, depositional bed forms (i.e., ripples and dunes) are ubiquitous—ranging in grain size from silt to gravel (Carling, 2005, 1999; Dinehart, 1992; Kleinhans, 2001; Kleinhans et al., 2002). These ubiquitous features can be quite complex, however, and this complexity helps further obfuscate our understanding of bed form dynamics. These complex dynamics are the result of, and a key boundary condition for, the bed load transport field.

The complexity of bed forms is apparent on large, multibed form scales in numerous ways. More often than not bed forms stray from the classically envisioned (i.e., simplified) two-dimensional, angle-of-repose bed form structure. Instead, bed forms tend to manifest in more complex ways such as low-angle bed forms or with highly three-dimensional crescentic, barchanoid, or irregular planform geometries (Allen, 1966; Bagnold, 1941; Best, 2005; Rubin, 2012; Venditti et al., 2005). The presence of bed forms on a river bed causes mean flow characteristics, bed shear stresses, and turbulent flow structures to differ significantly from those over flat beds (Best, 2005). Low-angle dunes may have no, or intermittent flow separation (Kwoll et al., 2016). Adding to the complexity, bed forms are frequently changing in space and time due to translation and deformation. Translation refers to the mean streamwise movement of the bed, whereas deformation is the change in the profile of a bed form in the translating frame of reference (McElroy & Mohrig, 2009). As bed forms deform spatially and temporally, so too do flow characteristics and near-bed shear stress distributions. Thus, bed load transport in any natural system cannot be fully understood without a comprehensive understanding of near-bed velocity and bed shear stress distributions at the scale of a single bed form.

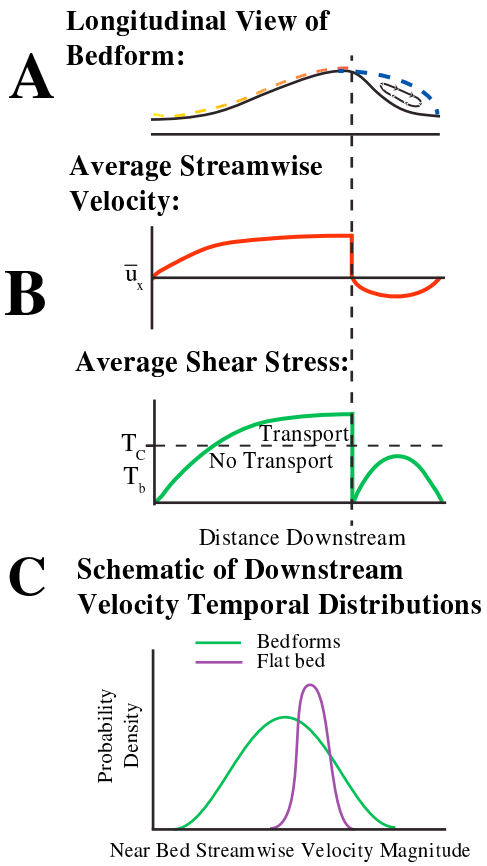

Figure 1. (a) Schematic of simplified flow dynamics over bed forms. Flow separates at the crest of each bed form and reattaches downstream (blue dashed line). Upon reattachment, flow accelerates up the bed form (red and yellow dashed line) before detaching at the crest of the next. (b) Schematic of temporally averaged streamwise velocity and shear stress values with distance along the bed form profile illustrated in Figure 1a. Horizontal dashed line shows region of predicted transport if temporally average values are used for transport equations that rely on average shear stress exceeding a critical shear stress. Vertical dashed line shows flow separation point. (c) Schematic of temporal distributions of streamwise fluid velocity for a flat bed and a bed with bed forms at a given point along the bed.

Even for the case of a nondeforming angle-of-repose bed form, the flow and bed load transport field is complex. The general features of flow over dunes (simplified from Best, 2005) is as follows: dune formation initiates flow separation on the lee side of the bed form; approximately 4–6 dune heights downstream, the flow reattaches (Engel, 1981). At this point, flow accelerates up the stoss side of the next bed form and reaches maximum streamwise velocity at the crest before separating and repeating the process (Figure 1a; Best, 2005).

Historically, these complexities of flow separation/reattachment and reacceleration have been dealt with by simply using spatial averages of mean flow characteristics (e.g., Smith & McLean, 1977) and standard bed load transport formulas that work best for uniform beds, such as the Meyer-Peter and Müller (1948) (MPM) equation (Wong & Parker, 2006). The MPM uses spatially averaged near-bed fluid velocities to calculate near-bed shear stress. This treatment of the inherent complexities of bed load transport over bed forms oversimplifies the problem and likely introduces sizeable error because mean flow characteristics change significantly spatially (Figure 1b).

Flow separation in the lee side of bed forms and flow reattachment and reacceleration on the stoss side of bed forms cause complex interactions between the flow, bed forms, and bed load sediment. Flow separation, reattachment, and reacceleration change the overall spatial distribution of fluid velocities interacting with the bed (Best, 2005), which in turn changes the spatial distribution of shear stress acting upon the bed (Figure 1b). Additionally, flow separation, reattachment, and reacceleration change the temporal distribution of near-bed fluid velocities at any given distance along the bed form profile (Figure 1c). Instead of being a narrow distribution that is characterized fairly well by the mean, flow separation and acceleration over bed forms increase the dispersion of the fluid velocity distribution and shear stress distributions (Figure 1c; Emadzadeh & Cheng, 2016; Jovic & Driver, 1994; Kwoll et al., 2016; Le et al., 1997; Nelson et al., 1995). Due to greater dispersion, it is possible to have both a mean shear stress that is below the critical shear stress as well as events that exceed that same critical shear stress (Figure 1c). This is a problem if one is using spatially or temporally averaged values and traditional bed load transport equations that rely on an average near-bed shear stress exceeding some theoretical critical shear stress to indicate initiation of transport. If we assume a steady flow and think of the profile of a bed form, as shown in Figure 1a, such an approach (i.e., near-bed shear stress exceeding the critical shear stress) only predicts transport on a portion of the stoss side of the bed form (Figure 1b).

Investigations into this oversimplification conducted by McLean et al. (1994, 1999a) and Nelson et al. (1993) found that the spatial averaging approach was indeed misleading because bed load transport varied distinctly at different locations along the bed form. However, the alternative approaches presented, namely, by McLean et al. (1999a, 1999b), suggested only using the portion of the dune where mean flow characteristics were similar to those of a uniform bed (i.e., at the dune crest) to estimate bed load transport. Although this kind of approach does eliminate some sources of error of spatial and temporal averaging methods, it does not provide a means of calculating the sediment transport rate at any location on a bed form. This local, sub–bed form sediment transport field is required to calculate the morphodynamics of bed forms using a suitable sediment continuity (Exner) equation.

Recent progress using turbulence- and particle-resolving numerical modeling of bed forms does not rely on bed load transport equations. Rather, only a force coupling between particles and flow is needed. Finn et al. (2016) used a LES-DEM (large eddy simulation and distinct element method) to generate ripples under oscillatory waves. Kidanemariam and Uhlmann (2014a, 2014b) used a fully resolved turbulence and DEM model

to generate small ripples. As such their model did not require an empirical particle/fluid force relationship. Sun et al. (2016) used an LES-DEM model nearly identical to Schmeeckle's (2014, 2015] model to generate bed forms in a unidirectional current. These important advances demonstrate that bed form generation directly from numerical simulation of turbulence and particle motion is now possible and a practical method for future investigations. However, none of these studies provide a spatiotemporal analysis of the pattern of bed load transport.

Following the work of Nelson et al. (1995), we explore the sub–bed form scale by taking a piece-wise approach to understanding the complexities associated with bed load transport over bed forms. Rather than assessing both flow separation/reattachment and flow reacceleration simultaneously, the study outlined herein investigates only the effects of flow separation/reattachment on downstream fluid and sediment dynamics. Does flow separation and reattachment give rise to specific fluid and bed load characteristics that are distinct from those of flat beds? Nelson et al. (1995) first investigated the effects of flow separation and reattachment with a series of experiments that were conducted using a backward facing step to initiate flow separation and in which bed load flux and flow velocities were measured at a series of distances downstream. Using quadrant analysis of flow velocity fluctuations, Nelson et al. (1995) demonstrated that near-bed shear stress could not fully account for the increase in transport downstream of the backward facing step. However, the mechanism responsible for this discrepancy remained unresolved.

The present study largely replicates the experiments of Nelson et al. (1995) using new technology and methodologies. In addition to comparing data to the results of Nelson et al. (1995), experimental data are compared to numerical model results of Schmeeckle (2015) in which turbulence and bed load transport downstream of a backward facing step were modeled simultaneously using a LES-DEM. Our goal is to elucidate details of the temporal and spatial pattern of bed load transport downstream of reattaching flow.

2. Methods

2.1. Experimental

Experiments were conducted in an 8.5 × 0.3 m recirculating flume whose bed was lined with sheets of plastic upon which sand was glued. A slot was cut into the plastic sheet (approximately 40 × 25 cm) in which a mobile bed of sand was placed. The immobile and mobile sand was well sorted with a median diameter of 0.05 cm. Two synchronized high-speed video cameras operating at 250 frames/s simultaneously observed motion of the bed load, illuminated by high-intensity LED lights, and the motion of neutrally buoyant particles illuminated by a laser light sheet parallel to and 6 mm above the mobile bed (Figure 2). The two high-speed cameras were synchronized so that the PIV camera triggered the bed load camera and the high-intensity LED lights that illuminated the bed. This allowed for synchronous data acquisition of both the fluid and the bed load. The field of view for both cameras was approximately 36 cm^2 with a resolution of 1280 × 1024 pixels. Images were captured of the mobile bed area downstream of a 3.81 cm tall backward facing step constructed of two 1.5 × 0.1905 m steel plates placed on top of on another (Figure 2). The height of this backstep was chosen so as to produce flow separation at the scale of a ripple and to replicate, as near as possible, the experiments of Nelson et al. (1995). Synchronized cameras, LED lights, and the laser were held in a fixed position over the mobile bed section, while the backstep was moved varying distances upstream in the flume. Data were collected at nine different distances downstream of the backward facing step (Table 1). The flow depth over the test section ranged from 17.4 to 17.8 cm depending on the run. The 4 mm range in flow depths is most likely due to small disturbances on the water surface. Bed load consisted of uniform, medium-sized sand particles with the median grain size (D_{50}) of 0.05 cm. The sand used is filter grade such that all particle diameters are between 0.045 cm and 0.055 cm.

The following experimental procedure was used for each run: first, the backstep was set to the desired distance upstream of the field of view. With the flume off, sand was loaded to the mobile bed and screeded to be flush with the surrounding fixed bed. Once the mobile bed was planar, a sheet of Plexiglas with a centimeter ruler grid printed on it was placed on top the mobile bed so that the mobile bed would stay intact until the beginning of recording. The flume was turned on and the flow rate was gradually raised to approximately 0.015 m^3/s. The speed of the electric motor pump is controlled by an inverter. The same volume of water was maintained in the tail tank to ensure that using an inverter rate of 54 Hz for each run would result in the same discharge. At the set discharge, a Plexiglas box was lowered within the flume to rest on the water surface above the mobile bed. This Plexiglas window provided optimal image clarity by minimizing distortions caused

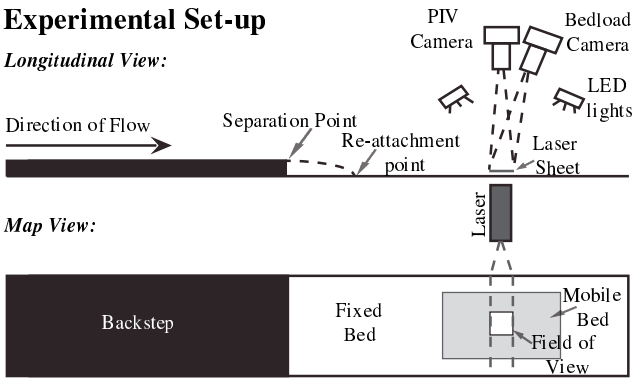

Figure 2. Schematic of experimental setup.

by an irregular water surface. We do not expect this window to affect either the near-bed fluid flow or the bed itself because it was barely submerged in the water and was 17 cm above the area of interest. The cameras and LED lights, mounted to a stable platform, were then moved into place above this window. The bed load and PIV cameras were adjusted to maintain the same field of view and focused on the bed load grid and the neutrally buoyant particles, respectively. Once focused, an image of the Plexiglas grid was taken for the PIV postprocessing. Once the computer interface was prepared for data acquisition, the Plexiglas grid was pulled from the mobile bed segment. As soon as the grid was completely removed from the mobile bed and the bed regained equilibrium, the PIV camera began recording; this triggered the bed load camera to begin recording. Run time ranged from 7.98 s (1,997 images) to 19.65 s (4,912 images) depending on the run.

One final run without mobile bed load was conducted in which Acoustic Doppler Velocimetry (ADV) data were collected at 25 distances downstream of the backstep at 5 cm intervals; each measurement was taken 1 cm above the bed for approximately 5 min. Data were recorded using a 200 Hz sampling rate, resulting in approximately 60,000 velocity readings per run. ADV correlation values, which are a measure of the signal quality in percentage, average 91.6%, 94.0%, and 91.0% for the velocities measured in the streamwise, cross-stream, and vertical directions, respectively. The mobile bed segment was replaced with an immobile bed (sheet of plastic upon which sand was glued) so as to avoid any scouring that may affect turbulence characteristics measured by the ADV. These data provide further streamwise, cross-stream, and vertical fluid velocity data. ADV was particularly useful in close proximity to the backstep where PIV was less accurate due to vertical fluid velocity fluxes moving neutrally buoyant particles in and out of the laser sheet.

2.2. Bed load Transport Rate Measurement and Calculations

Bed load movement analysis was conducted using bed load images and the open-source software ImageJ (discussed in detail in section 2.3; Meijering et al., 2012). Bed load transport rates were acquired by manually tracking sand particles as they crossed a 6 m line bisecting the field of view (discussed in detail in section 2.3). Particle imaging velocimetry (PIV) algorithms were applied to the laser sheet images to obtain two-dimensional field of two-dimensional vectors that describe fluid motions (discussed in detail in section 2.4).

To assess the effect of flow separation and reattachment on bed load transport, bed load transport is estimated as a function of near-bed shear stress and compared to measured values. Previous research has shown that common bed load transport equations, which are functions of boundary shear stress, work poorly in flows where the turbulence intensity is increased relative that found in flow over a flat boundary (Nelson et al., 1995; Sumer et al., 2003). Thus, agreement between these measured and calculated values of bed load transport are not expected, but the magnitude and spatial pattern of the discrepancy are expected to elucidate how transport differs downstream of the step relative to more simple flows.

Table 1
Summary of Experimental Results

Run	Distance downstream (cm)	Distance downstream (step heights)	$q_s\left(\frac{\text{grains}}{\text{cm*s}}\right)$	$q_s\left(\frac{\text{cm}^2}{\text{s}}\right)$
1	130	34.12	13.5	0.00088
2	115	30.18	10.3	0.00067
3	100	26.24	12.3	0.0008
4	85	22.3	9.2	0.0006
5	70	18.37	6.8	0.00044
6	55	14.44	8.6	0.00056
7	40	10.5	3.1	0.0002
8	25	6.56	6.1	0.00039
9	15	3.93	−4.5	−0.00029

Table 2
Summary of Calculated Bed Load Transport Results

Distance downstream (cm)	Distance downstream (step heights)	$\overline{u}$ (cm/s)	u_* (cm/s)	τ_*	q_*	$q_{sm}\left(\frac{cm^2}{s}\right)$
10	2.62	−5.15	0.31	0.0011	0	0
15	3.94	−4.27	0.26	0.0008	0	0
20	5.25	−3.64	0.22	0.0005	0	0
25	6.56	−0.26	0.02	0.00003	0	0
30	7.87	3.28	0.2	0.0005	0	0
35	9.19	6.39	0.39	0.0018	0	0
40	10.5	8.37	0.51	0.0032	0	0
45	11.81	11.14	0.68	0.0058	0	0
50	13.12	9.81	0.6	0.0044	0	0
55	14.44	8.27	0.5	0.0031	0	0
60	15.75	8.31	0.51	0.0032	0	0
65	17.06	12.28	0.76	0.0071	0	0
70	18.37	11.82	0.73	0.0065	0	0
75	19.69	15.35	0.94	0.0109	0	0
80	21	15.84	0.97	0.0116	0	0
85	22.3	21.02	1.27	0.0199	0	0
90	23.62	24.38	1.46	0.0264	0	0
95	24.93	25.75	1.54	0.0294	0	0
100	26.25	26.53	1.59	0.0311	0	0
105	27.56	27.06	1.62	0.0323	0.000011	0.000004
110	28.87	27.44	1.64	0.0332	0.0001	0.00004
115	30.18	26.96	1.61	0.0321	0.000001	0.0000005
120	31.5	28.5	1.69	0.0357	0.0006	0.00028
125	32.8	28.9	1.72	0.0366	0.0009	0.0004
130	34.12	29.27	1.74	0.0375	0.0012	0.00054

Note. Calculated bed load transport was predicted using Acoustic Doppler Velocimetry data and a modified MPM equation from Wong and Parker (2006). $\tau_{*c} = 0.032$.

In this subsection we compare measurements of bed load transport to bed load transport calculated using time-averaged measures of boundary shear stress. Experimentally observed bed load transport (q_s) was measured by tracking grains of sand as they passed over a 6 cm line in the middle of the field of view. For calculated bed load transport, we use the law of the wall to derive the temporally averaged bed shear stress and a modified MPM equation from Wong and Parker (2006) to estimate bed load transport.

Does our technique work well using the law of the wall to relate mean velocity to stress? This technique does not rely on the profile from the bed to the point of measurement actually being logarithmic; rather, the question is whether the relationship between mean velocity at the point of measurement and stress at the bed is nearly the same as that of the law of the wall. The DNS simulations of Le et al. (1997) and experiments of Jovic and Driver (1994) for flow over a backward facing, smooth-walled step illustrate that the relationship between mean velocity and stress downstream of a backward facing step is nearly the same as that of the law of the wall at certain points of measurement. Velocity profiles at varying distances downstream of a backward facing step from Le et al. (1997) show a log linear zone extending from approximately 10 to 100 wall units. Our estimates of $u/u*$ at 100 wall units (1 cm; Table 2) are in agreement with the log linear zone outlined in Le et al. (1997). This log linear zone, however, is somewhat suppressed below the standard law of the wall due to an adverse pressure gradient with the percent error being approximately 17% (Le et al., 1997). We expect the possible percent error for the experiments presented herein to be similar to that of Le et al. (1997). Although there may be some error, using the law of the wall method for the experimental setup presented herein should provide a reasonable estimate of the local, time-averaged boundary shear stress.

ADV data were used to predict bed load transport rates. ADV measurements yield time-averaged streamwise velocity values ($\bar{u}$) that can be used to derive near-bed shear stress using the following equations. Shear velocity (u_*) was calculated using the law of wall:

$$\bar{u} = \frac{u_*}{k} \ln\left(\frac{z}{z_0}\right) \tag{1}$$

where k is von Kármán's constant (0.41), z is the distance above the bed (1 cm), and z_0 is the distance from the boundary at which the idealized velocity given by the law of the wall goes to zero. The empirical fit of Duan (2004) to the data of Nikuradse (1933) provides an estimate of this length scale:

$$z_0 = D_{50}\left(0.0275 - 0.007\sqrt{\sin\left(\frac{R_e - 4}{4}\right)\pi}\right) \tag{2}$$

where D_{50} is the median grain size (0.05 cm) and R_e is the boundary Reynolds number. Equation (2) is applied to transitionally rough boundaries with Re between 4 and 11. Equation (1) can be reorganized to solve for shear velocity:

$$u_* = \frac{\bar{u}k}{\ln\left(\frac{z}{z_0}\right)} \tag{3}$$

Using shear velocity acquired from equation (3), near bed shear stress (τ_b) is calculated:

$$\tau_b = \rho u_*^2 \tag{4}$$

where ρ is fluid density. Near-bed shear stress is then nondimensionalized:

$$\tau_* = \frac{\tau_b}{(\rho_s - \rho)gD_{50}} \tag{5}$$

Where ρ_s is the density of the sediment(2.65 g/cm^3), ρ is the density of the fluid (1 g/cm^3), and g is gravitational accelleration. Nondimensional sediment transport (q_*) is solved for using a modified MPM equation from Wong and Parker (2006):

$$q_* = 4.93(\tau_* - \tau_{*c})^{1.6} \tag{6}$$

which is evaluated for conditions of $\tau_* > \tau_{*c}$, where τ_* is the nondimensional near-bed shear stress and τ_{*c} is the nondimensional critical shear stress calculated from the Shields (1936) diagram. If $\tau_* < \tau_{*c}$, q_* is expected to be zero. Calculated, dimensional bed load transport (q_{sm}; cm^2/s) is calculated by:

$$q_{sm} = q_* D_{50}\sqrt{\left(\frac{\rho_s - \rho}{\rho}\right)gD_{50}} \tag{7}$$

Table 2 contains all values obtained through these calculations. Using data from Roseberry et al. (2012) in which bed load transport was observed over a flat bad in the same flume and using the same sediment used herein, we demonstrate that calculating sediment transport using the above methodology reasonably approximates observed bed load transport (supporting information Figure S1).

2.3. Determining Patterns of Transport

Detailed streamwise and cross-stream bed load flux time series data, coupled with manual particle tracking of bed load sand grains, are used to assess changes in bed load transport patterns downstream of the region of flow separation. First, bed load flux time series were calculated by manually tracking grains that cross over a 2 cm vertical line (i.e., perpendicular to the direction of flow; herein reported as streamwise flux) and a 2 cm horizontal line (i.e., parallel to the direction of flow; herein reported as cross-stream flux) located in the middle of the field of view on the experimental bed load images at all nine distances downstream of the backward facing step included in Table 1. Particles were counted at 0.1 s intervals for the first 8 s of each experimental run (supporting information Figure S3).

Although 8 s is a short sample time, obtaining these data of transport rates is laborious and tedious, requiring hundreds of hours. Direct estimates of standard errors of statistics obtained from these samples is difficult because of serial correlation. We can, however, reliably estimate standard errors of 8 s samples of the 3,000 s velocity measurements, as an indication of errors expected for the sediment transport rates. We calculate

the mean and standard deviation of each 8 s window in the 3,000 s velocity time series. The standard deviation of these window means and standard deviations provides estimates of the standard errors of the mean and standard deviation. The standard error of the mean and the standard error of the standard deviation of the 8 s samples were both found to be less than or equal to 10% of the standard deviation of the 3,000 s velocity time series. Bed load concentration is more variable than near-bed velocity. Hence, we expect standard errors of measured sediment transport rates to be somewhat higher than 10% of the standard deviation.

Periods of high streamwise and cross-stream flux were then selected for detailed manual particle tracking analysis at distances 6.56, 14.44, and 30.18 step heights downstream of the backstep. Particle tracking of high flux events was conducted using the MTrackJ plugin for ImageJ (Meijering et al., 2012). This tool allows for manual particle tracking of individual grains through time by using a cursor to select the center of a grain at a given point in time. Once the center of the grain is selected, the tool advances to the next frame in time where the center of the grain is manually selected again. For each event, ~250–500 grains were tracked from initiation of movement to completion of movement/exiting the field of view (supporting information Movies S1–S3). Length of transport, average and instantaneous particle velocity, and average and instantaneous direction of particle transport were recorded for each grain. Direction of particle transport is defined in terms of degrees where 0 to $-/+20°$ is streamwise transport, $-/+20$ to $-/+90°$ is left lateral and right lateral transport, respectively, and $-/+180$ is transport in the upstream direction. Directions of transport reported anywhere in between these values contain components of both streamwise and cross-stream transport.

2.4. Determining Flow Patterns

Bed load flux time series and manual particle tracking data were then coupled with fluid velocity data acquired by the ADV. Unfortunately, the quality of PIV data collected are quite poor, especially for runs 1–4 (Table 1) near flow reattachment (supporting information Figure S2). This reduction in PIV data quality is likely due to significant vertical fluid velocities moving neutrally buoyant particles in and out of the laser sheet. Significant exiting and entering of neutrally buoyant particles reduces the accuracy of the PIV algorithms because those particles cannot be tracked in the next time step. We thus rely primarily on the ADV data collected to analyze patterns of turbulence.

ADV fluid velocity data were analyzed qualitatively with Quantile-Quantile (Q-Q) plots (supporting information Figure S4) and quantitatively using percentile differencing. Quantiles (similar to percentiles) are the proportion of data that fall below a certain point (i.e., 0.5 quantile is equal to the 50th percentile and indicates 50% of the data are less than that corresponding value). In a bell curve standard normal distribution, the mean value is 0 and corresponds to the 0.5 quantile. A Q-Q plot is a graphical tool for comparing two distributions. For the analysis herein, fluid velocity distributions are compared to a theoretical normal distribution. Sample data (i.e., fluid velocities) are sorted in ascending order and then plotted versus a theoretical normal distribution. In this case, the normal distribution has a mean of 0 (0.5 quantile) and a standard deviation of 2. The solid, black line on each Q-Q plot in supporting information Figure S4 indicates where the sample data should plot if the sample data are normally distributed. Any divergence from this line indicates that the distribution is not normal.

Q-Q plots shown herein show distinct changes in the distribution of streamwise, cross-stream, and vertical fluid velocities with increasing distance downstream from the backstep (supporting information Figure S4). In all the Q-Q plots shown in supporting information Figure S4, the distributions display heavy tails. However, the tails of each distribution became less heavy, compared to the normal distribution, with increasing distance downstream.

To quantify this change, we use the below percentile differencing for the positive tail:

$$\frac{99\text{th} - 50\text{th}}{\text{SD}} \tag{8}$$

and

$$\frac{1\text{st} - 50\text{th}}{\text{SD}} \tag{9}$$

for the negative tail, where SD is the standard deviation of the distribution. This percentile differencing approach highlights changes in the tails of distributions. For example, if the 1st and 99th percentiles of a distribution increase in magnitude (with respect to the mean) with increasing distance downstream from the backstep, the distribution would become more dispersed and we expect equations (8) and (9) to diverge

Table 3
Summary of Percentile Differencing Results

Distance downstream (cm)	Distance downstream (step heights)	$\frac{U_x}{\frac{99th-50th}{SD}}$	$\frac{U_x}{\frac{1th-50th}{SD}}$	$\frac{U_y}{\frac{99th-50th}{SD}}$	$\frac{U_y}{\frac{1th-50th}{SD}}$	$\frac{U_z}{\frac{99th-50th}{SD}}$	$\frac{U_z}{\frac{1th-50th}{SD}}$
15	3.94	2.62	−2.39	2.47	−2.44	2.17	−3.05
25	5.25	2.80	−2.13	2.65	−2.38	1.95	−2.99
40	10.5	3.02	−1.86	2.43	−2.40	1.95	−3.02
55	14.44	2.91	−1.90	2.65	−2.34	2.27	−2.78
70	18.37	2.88	−1.88	2.51	−2.48	2.54	−2.53
85	22.31	2.78	−1.86	2.42	−2.38	2.31	−2.73
100	26.25	2.67	−1.95	2.45	−2.32	2.35	−2.63
115	30.18	2.61	−1.96	2.48	−2.32	2.38	−2.67
130	34.12	2.55	−2.01	2.49	−2.30	2.39	−2.62

Note. Percentile differencing (equations (8) and (9)) of streamwise (U_x), cross-stream (U_y), and vertical (U_z) fluid velocities.

from zero. If the 1st and 99th percentiles of a distribution decrease in magnitude (with respect to the mean) with increasing distance from the backstep, the distributions would become less dispersed and we expect equations (8) and (9) to approach zero. Table 3 contains values calculated using equations (8) and (9) for streamwise, cross-stream, and downstream fluid velocities.

2.5. ADV Octant Analysis

To analyze fluid velocity patterns in further detail, octant analysis was conducted at three distances downstream of the backstep: 6.56, 14.44, and 30.18 step heights. Octant analysis, the three-dimensional version of quadrant analysis, separates the flow into eight regions defined by fluid fluctuations in the streamwise, vertical, and cross-stream directions (Table 4; Keylock et al., 2014, Madden, 1997). Fluid velocity fluctuations are defined as

$$u_i' = u_i - \bar{u}_i \tag{10}$$

where u' is the magnitude of the fluid velocity at a given point in time (u_i) deviates from the mean ($\bar{u}_i$). The subscript "i" denotes the direction of flow (streamwise (x), cross-stream (y), or vertical (z)). Quadrant (two-dimensional) analysis and octant (three-dimensional) analysis can be conducted by pairing these downstream and vertical fluctuations (quadrant analysis) or downstream, cross-stream, and vertical fluctuations (octant analysis; Table 4). The analysis presented herein utilizes octants.

These octants describe the instantaneous direction of fluid movement at a given point in time and correspond to the traditional flow events: sweep, bursts, outward interactions, and inward interactions (Table 4). Keylock et al. (2014) illustrated that octant analysis can be paired with Markovian transition probability analysis to identify significant fluctuation sequences in the flow. Markov transition analysis is dependent of the existence of a Markov Chain, which is defined as a series of states transitioning from one another such that $S = \{s1, s2, s3, \ldots, sn\}$, where S indicates the sequence and $s1$ to sn are the constantly transitioning states. Markov transition probabilities indicate the probability an object in the theoretical state "$s1$" will transition to the theoretical state "$s2$" (Grinstead & Snell, 2012). Applying this to a time series of octants, one can extract the probabilities of fluid flow transitioning from one octant to another. These probabilities are illustrated using Markov transition matrixes (Tables 5–7).

Table 4
Summary of Octants

Quadrant	Quadrant name	U_x	U_z	Octant	U_y
1	Outward interaction	>0	>0	+1	<0
				−1	>0
2	Burst	<0	>0	+2	<0
				−2	>0
3	Inward interaction	<0	<0	+3	<0
				−3	>0
4	Sweep	>0	<0	+4	<0
				−4	>0

Note. Modified from Keylock et al. (2014).

ADV fluid velocity data at 6.56, 14.44, and 30.18 step heights were converted into time series of octants. These octant time series were then used to calculate Markov transition matrixes. Tables 5–7 show the probability of each octant transitioning to each other octant at 6.56, 14.44, and 30.18 step heights, respectively. These probabilities were then used to identify primary, secondary, and tertiary (all three only at 6.56 step heights) octant sequences. Sequences are denoted with {…}. The highest probable sequences of transitions at each distance are classified

Table 5
Octant Transition Probability Matrix at 6.56 Step Heights

Octants	−4	−3	−2	−1	+1	+2	+3	+4
−4	0.000	**0.348**	0.037	0.228	0.019	0.001	0.038	***0.327***
−3	**0.391**	0.000	**0.291**	0.045	0.003	0.014	0.213	0.043
−2	0.040	0.214	0.000	**0.410**	0.043	**0.263**	0.025	0.005
−1	0.238	0.040	**0.413**	0.000	0.224	0.046	0.006	0.032
1	0.040	0.004	0.042	0.232	0.000	**0.328**	0.044	***0.309***
2	0.004	0.020	**0.278**	0.054	**0.330**	0.000	0.263	0.051
3	0.039	0.185	0.015	0.004	0.032	0.263	0.000	**0.462**
4	***0.271***	0.032	0.001	0.019	0.214	0.041	**0.420**	0.000

Note. Rows are octant origins and columns are octant destinations. Bold indicates primary sequences, italic indicates secondary sequence, and bold underline indicates tertiary sequences.

as "primary sequences." These sequences were identified by first identifying the most likely transition of all the octants. For example, lets say the most probable transition is {−3 −2} at 0.412. This would be the beginning of our sequence. We would then go to −2 and find the most probable transition it would take, in this case +2. We repeat this process until the sequence either repeats (in this case, comes back to −3) or stagnates by continuously repeating between two octants.

At 6.56 "secondary sequences" were identified by assuming the primary sequences did not occur but assuming the next highest probable transitions did. "Tertiary sequences" were identified in a similar manner: by assuming neither the primary nor secondary sequences occurred but that the next highest probable transition did occur. Using this Markovian transition probability analysis, we can see how the fluid flow evolves with increased distance downstream of the backstep.

2.6. Octant Analysis of Numerical Splat Events

Since experimental data reported herein do not contain sufficient coupled bed load and fluid velocity measurements (due to the poor quality of the PIV data), we aim to shed light on the potential coupling of data reported herein by utilizing data from the numerical simulations of Schmeeckle (2015) of nearly the same geometry reported here. Fluid flow and bed load movement over and downstream of a 4 cm high backward facing step were modeled using the large eddy simulation (LES) and distinct element method (DEM), respectively. LES and DEM models are coupled in momentum. The computational domain began at the backward facing step and extended 1.2 m downstream (30 step heights). This domain extended 0.1 m (2.5 step heights) in the cross-stream direction. Data were collected in 0.01 m × 0.01 m grid cells. Fluid velocities, shear stress, and particle movement were recorded at 40 Hz (every 0.025 s). For a complete description of this methodology, please refer to Schmeeckle (2015).

Of particular interest are the presence and importance of spat events, as noted by Schmeeckle (2015). Perot and Moin (1995) were the first to discuss the process of splat events in which fluid impinges on an

Table 6
Octant Transition Probability Matrix at 14.44 Step Heights

Octants	−4	−3	−2	−1	+1	+2	+3	+4
−4	0.000	0.270	0.125	0.181	0.032	0.022	0.035	**0.335**
−3	0.325	0.000	**0.412**	0.082	0.010	0.049	0.079	0.042
−2	0.134	0.254	0.000	0.225	0.038	**0.300**	0.030	0.020
−1	0.365	0.102	0.299	0.000	0.095	0.055	0.014	0.070
1	0.061	0.013	0.044	0.084	0.000	0.313	0.081	**0.403**
2	0.024	0.031	0.273	0.044	**0.296**	0.000	0.196	0.135
3	0.050	0.077	0.071	0.013	0.093	0.384	0.000	0.312
4	**0.346**	0.031	0.018	0.033	0.234	0.117	0.221	0.000

Note. Rows are octant origins and columns are octant destinations. Bold indicates primary sequence.

Table 7
Octant Transition Probability Matrix at 30.18 Step Heights

Octants	−4	−3	−2	−1	+1	+2	+3	+4
−4	0.000	***0.361***	0.046	0.137	0.0237	0.008	0.055	**0.369**
−3	0.254	0.000	**0.458**	0.034	0.005	0.068	0.154	0.026
−2	0.056	0.220	0.000	0.306	0.051	**0.338**	0.022	0.008
−1	0.361	0.050	0.219	0.000	0.262	0.038	0.008	0.064
1	0.074	0.010	0.028	0.221	0.000	0.230	0.056	**0.380**
2	0.013	0.033	0.308	0.053	**0.392**	0.000	0.146	0.055
3	0.043	0.171	0.062	0.009	0.045	0.421	0.000	0.250
4	**0.389**	0.053	0.009	0.026	0.196	0.046	0.281	0.000

Note. Rows are octant origins and columns are octant destinations. Bold indicates primary sequence.

impermeable boundary. Impingement of fluid causes the boundary normal velocity to stagnate and causes the impinging fluid to be redirected parallel to the boundary (Perot & Moin, 1995). Because the boundary in question for these experiments (sand) is a porous medium, fluid infiltrates into the very top portion of the bed in addition to simply being redirected parallel to the bed (Schmeeckle, 2015). To accommodate the increase of fluid in the bed, fluid exfiltrates in all directions around the point of infiltration. Sediment is ejected in all directions from the bed during exfiltration, thus initiating bed load transport. This coupled outward interaction and sweep in addition to the radial bed load transport pattern is known as a "permeable splat event," herein referred to simply as splat events (Figure 3; Schmeeckle, 2015). Stoesser et al. (2008) also noted the existence of splat events near flow reattachment in their numerical simulations of turbulence over dunes.

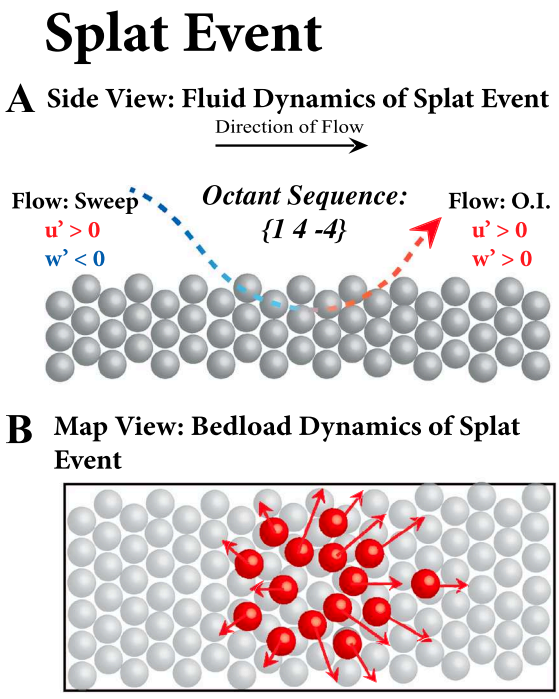

Figure 3. Schematic of fluid and bed load dynamics associated with a permeable splat event. (a) Flow characterized by positive streamwise velocity fluctuations and negative vertical velocity fluctuations (sweep turbulent structure) impinges on and penetrates into the bed. This causes exfiltration in all directions around the point of infiltration, characterize by flow with both positive vertical and streamwise velocity fluctuations (outward interaction, O.I., turbulent structure). (b) This initiates bed load transport by ejecting grains from the bed in all directions.

Six splat events from this numerical data were analyzed in detail (Table 8). Splat events were identified visually by noting localized areas of large streamwise and cross-stream transport 0–12 step heights downstream from the backstep. The spatial and temporal extent each splat event was identified. Fluid velocity fluctuations in the streamwise, cross-stream, and vertical directions were logged every 2 cm in the x direction and every centimeter in the y direction (Figure 4) at each time step. These fluctuations were then converted to octants. At each position and time step, near bed shear stress, streamwise transport, and cross-stream transport were also collected and paired with their respective octant for that position and time step. Using octants and bed load transport data from these splat events, we identify the octants responsible for bed load transport within a splat event.

3. Results

3.1. The Spatial Effects of Flow Separation and Reattachment

For the experiments described herein, flow reattachment occurs between 4.72 and 5.77 step heights. This was determined by the fact that bed load images collected at 3.94 step heights and 6.56 step heights do not show a region of zero transport anywhere within their field of view. Additionally, the bed load images collected at 3.94 step heights capture only negative streamwise transport whereas the bed load images at 6.56 step heights capture only positive streamwise transport (supporting information Figure S3). Since these distances refer to the center of the field of view on the bed load images, and the field of view is approximately 36 cm^2, we can surmise that the reattachment point must be somewhere between the most downstream point of the 3.94 step heights measurement location (i.e., 4.72 step heights) and the most upstream point of the 6.56 step heights measurement location (i.e., 5.77 step heights). This is congruent with where we would expect to see flow reattachment based on Engel (1981).

Table 8
Summary of Numerical Splat Events

Splat event	*Xbeg* (m)	*Xend* (m)	*Ybeg* (m)	*Yend* (m)	T_1 (s)	T_2 (s)	Duration (s)
1	0.2	0.27	0.06	0.09	1.625	1.775	0.15
2	0.4	0.45	0.06	0.09	3.1	3.35	0.25
3	0.21	0.27	0.07	0.09	3.5	3.85	0.35
4	0.18	0.24	0.06	0.09	4.2	4.35	0.15
5	0.27	0.33	0.03	0.05	9.375	9.55	0.175
6	0.31	0.37	0.04	0.09	17.45	17.6	0.15

Figure 5a shows bed load transport rates (Table 1) and fluid velocity downstream of a backward facing step. Fluid velocity and bed load flux monotonically increase downstream of the backward facing step. ADV fluid velocity data were used for this relationship rather than PIV fluid velocity data due to reduction in PIV data quality close to the backstep (supporting information Figure S2). In contrast to the findings presented herein, the results of Nelson et al. (1995) show a peak in transport approximately 20 step heights downstream of the backward facing step. In agreement with results presented herein, SchmeeckleŠs (2015) LES-DEM simulations of the same geometry of the Nelson et al. (1995) experiments did not show a peak in bed load transport.

Comparison of calculated and observed bed load transport shows that using near-bed shear stress to predict bed load transport underestimates bed load transport at all sampling distances downstream of the backward facing step (Figure 5b). In fact, the near-bed shear stress model predicts little to no bed load transport until approximately 27.5 step heights downstream, whereas observed bed load transport occurs at all distances downstream of the backstep. The discrepancy between calculated and observed bed load flux is most likely the result of the turbulent flow structures associated with flow separation/reattachment. To explore how these turbulent flow structures, and therefore bed load transport characteristics, are evolving with distance downstream, we selected three distances downstream of reattachment for the detailed fluid and bed load analyses

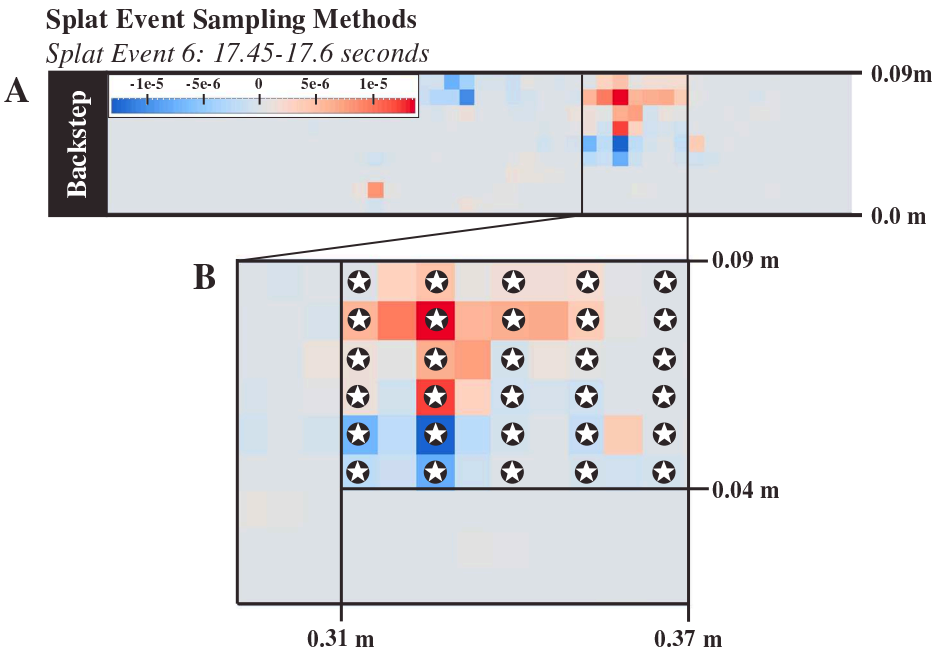

Figure 4. Schematic of sampling methodology for numerical splat analysis. (a) Map view of cross-stream transport (m^2/s) of splat event 6. (b) Grid of sampling locations (black circles with stars) for Splat Event 6. Each splat event was sampled using a similar grid: every 2 cm in the *x* direction and every 1 cm in the cross-stream direction. Octants, near-bed shear stress, streamwise transport, and cross-stream transport were collected at each location every 0.025 s (40 Hz).

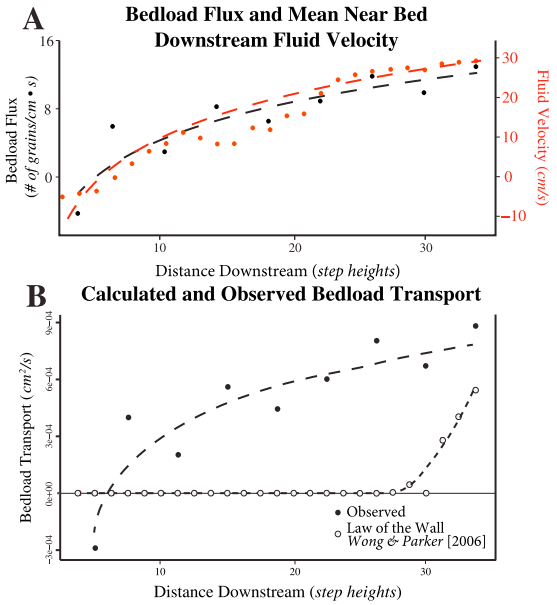

Figure 5. (a) Bed load flux and ADV flow velocity data (measured at 5 mm above the bed). Bed load flux covaries with fluid velocity, increasing nonlinearly downstream of a backward facing step. Dashed lines are fits to the data. (b) Calculated bed load transport compared to exerpimentally observed bed load transport. Calculated bed load transport underestimates observed bed load transport at all sample distances downstream of the backward facing step. Negative bed load flux values indicate transport in the upstream direction.

outlined in sections 2.3 and 2.5. The distances selected (6.56, 14.44, and 30.18) where chosen for their proximal, intermediate, and distal relationships with flow reattachment, respectively.

3.2. Fluid Velocity Patterns

3.2.1. Quantile-Quantile Analysis and Percentile Differencing

Temporal fluid velocity distributions show distinct differences with increasing distance downstream from the backstep (Figure 6 and supporting information Figure S4). Quantile-Quantile plots of streamwise, cross-stream, and vertical velocity distributions display heavier tails near flow reattachment than fluid velocity distributions further downstream (supporting information Figure S4). This indicates that large-magnitude fluid velocity fluctuations (in all directions) are more likely near flow reattachment than farther downstream.

In particular, near flow reattachment (0–14.44 step heights), 1th percentile of the vertical velocity and 99th percentile of the streamwise velocities are much larger than the median values of each (Figure 6a). Conversely, farther downstream, these values are still larger than the median value, as to be expected due to the fact that they are 1th and 99th percentiles; however, they are much closer in magnitude to the median value. Changes in 1th and 99th percentiles with respect to the mean suggest distinct changes in both vertical and streamwise velocity distributions (i.e., more dispersed distributions near flow reattachment).

Percentile differencing of streamwise fluid velocities (Figure 6b) shows that proximal to reattachment, large-magnitude positive streamwise (99th percentile) events peak at 10.50 step heights and then gradually diminish with distance downstream. This indicates that flow separation and reattachment

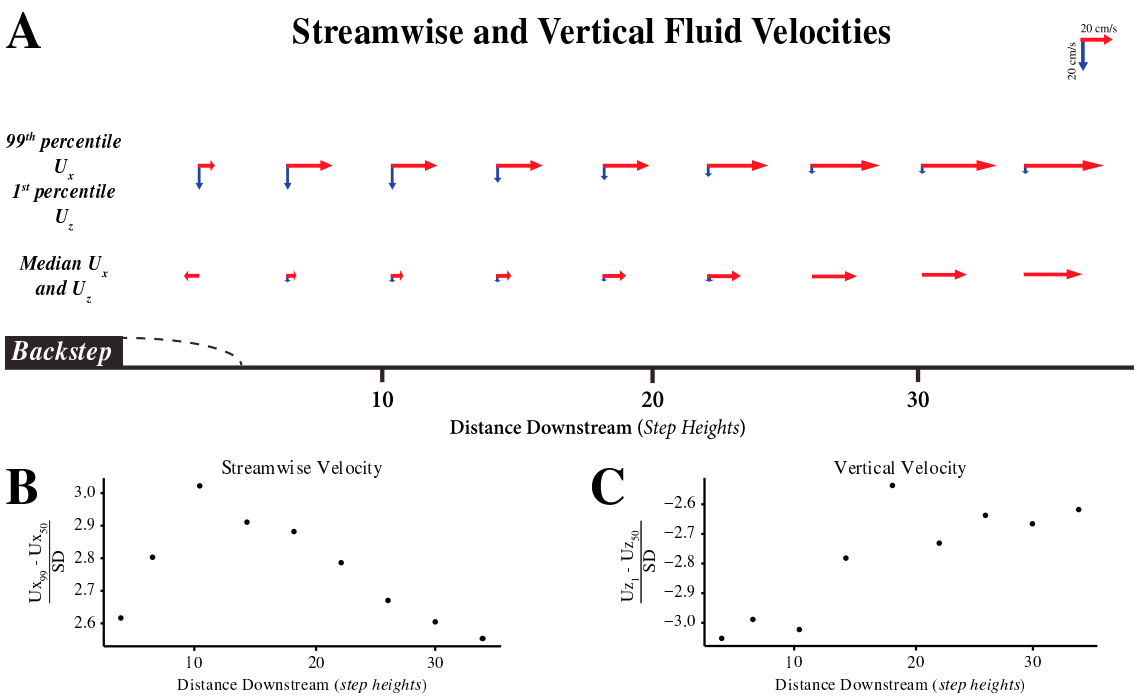

Figure 6. (a) Velocity vectors downstream of the backstep. Bottom row of vectors represents the median (50th percentile) values for both streamwise and vertical fluid velocities. The top row of vectors contains 99th percentile streamwise fluid velocities (i.e., large-magnitude positive streamwise velocity events) and 1st percentile vertical fluid velocities (i.e., large-magnitude negative vertical velocity events). (b) Percentile differencing (as defined in section 2.4) for the positive tail of streamwise velocity distributions. (c) Percentile differencing (as defined in section 2.4) for the negative tail of vertical velocity distributions.

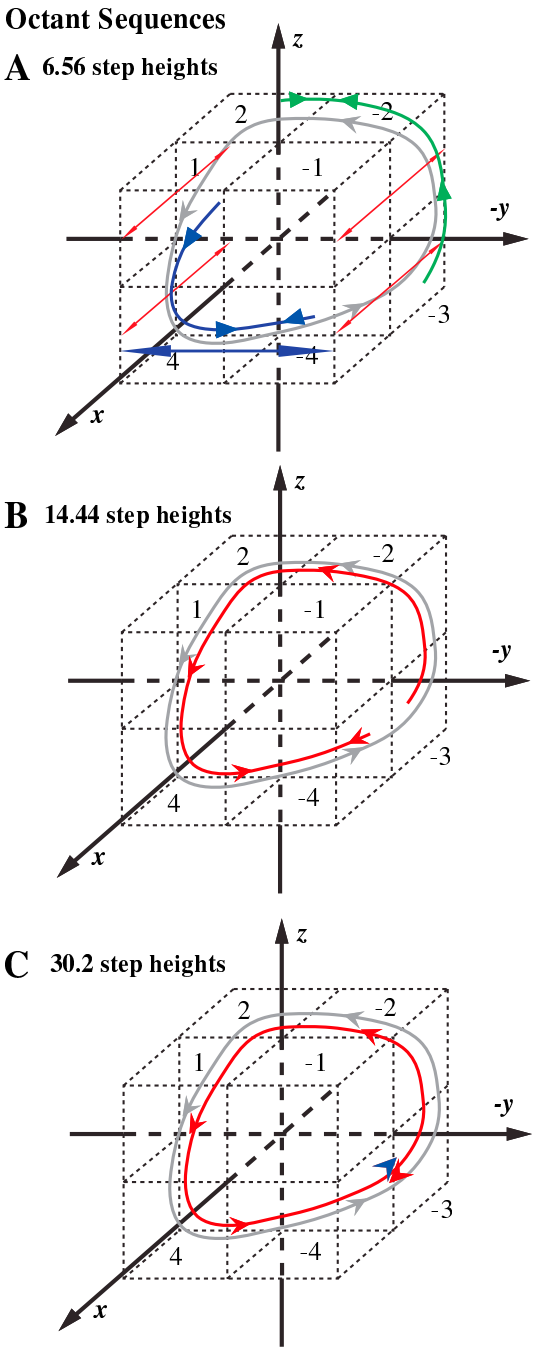

Figure 7. Schematic of primary (red), secondary (blue), and tertiary (green) octant transitions (modified after Keylock et al., 2014) for (a) 6.56, (b) 14.44, and (c) 30.2 step heights. The gray sequence shown in Figures 7a–7c is the primary octant transition sequence {−3 −2 2 1 4 −4} observed by Keylock et al. (2014). Portions of this sequence exist at all locations but are only primary transitions at 14.44 and 30.2 step heights. This sequence only repeats, however, at 30.2 step heights, where the probability of the {−4 −3} transition and the stagnating transition of {−4 4} are comparable (0.361 and 0.369, respectively). These two transitions are noted with blue and red arrows at the transition from octant −4 to octant −3.

play a role in boosting large-magnitude streamwise fluid events. Percentile differencing of vertical fluid velocity (Figure 6c) similarly shows an increase in large-magnitude negative vertical fluid velocity events near flow reattachment that diminishes with increased distance downstream. In addition to boosting large-magnitude streamwise velocity events, flow reattachment also appears to bring more fluid toward the bed proximal to reattachment (e.g., Bennett & Best, 1995).

This is congruent with our supposition that the quality of PIV data degrades near flow reattachment due to vertical fluid velocity moving particle in and out of the laser sheet. Where our PIV data quality is good (i.e., at 30.18 and 34.12 step heights) correlates to where vertical fluid velocity percentile differencing is lowest. In other words, where we see evidence for less negative vertical fluid velocity fluctuations, we also see a higher quality in PIV data. Where high magnitudes of vertical fluid are coming down into the bed, we see very poor quality PIV data (supporting information Figure S2).

3.2.2. Octant Analysis

Octant transition probabilities of fluid velocity octants at 6.56, 14.44, and 30.18 step heights (Tables 5–7, respectively) show in detail the evolution of fluid flow at varying distances downstream of flow reattachment. Similarly to Keylock et al. (2014), we see the development of a dominant, three-dimensional flow sequence: {−3 −2 2 1 4 −4}. This same sequence is identified by Keylock et al. (2014) as the second most probable six-octant sequence. This flow sequence exists in temporally intermittent segments near flow reattachment (6.56 step heights) and develops into a more coherent, cyclical sequence with increased distance downstream.

At 6.56 step heights, three distinct "levels" of flow are apparent: primary, secondary, and tertiary sequences. The primary sequences are composed of repeating fluctuations in the streamwise direction (Figure 7a and Table 5). The secondary sequences are composed of a horizontal transition between the +4 and −4 octants. This horizontal transition can also be accompanied by a vertical transition (in the negative direction) from the +1 to +4 octants ({1 4 −4}; Figure 7a and Table 5). This sequence is equivalent to outward interactions and sweep events and was identified by Keylock et al. (2014) as the most probable three-octant sequence. Keylock et al. (2014) also found that this sequence is extremely significant for bed load entrainment.

The tertiary sequence at 6.56 step heights is composed of a vertical transition (in the positive direction) from the −3 to −2 octants followed by a horizontal transition from the −2 to +2 octants ({−3 −2 2}; Figure 7a and Table 5). This sequence is equivalent to inward interactions and burst events and was identified by Keylock et al. (2014) as the third most probable three-octant sequence. Both the secondary and tertiary sequences appear to stagnate in the horizontal direction ({4 −4} and {−2 2}, respectively). In other words, the {1 4 −4} and {−3 −2 2} sequences appear to be temporally intermittent flow features as opposed to continuously cyclical flow features (Figure 7a).

At 14.44 step heights we begin to see the development of the {−3 −2 2 1 4 −4} sequence. This is the primary octant sequence at this distance. Although this is the most probable sequence, it is not a repetitive sequence. Rather, the end of the sequence is likely to stagnate in the horizontal direction ({−4 4}) rather than continuing on in a cyclical manner from octant −4 to octant −3 (Figure 7b and Table 6).

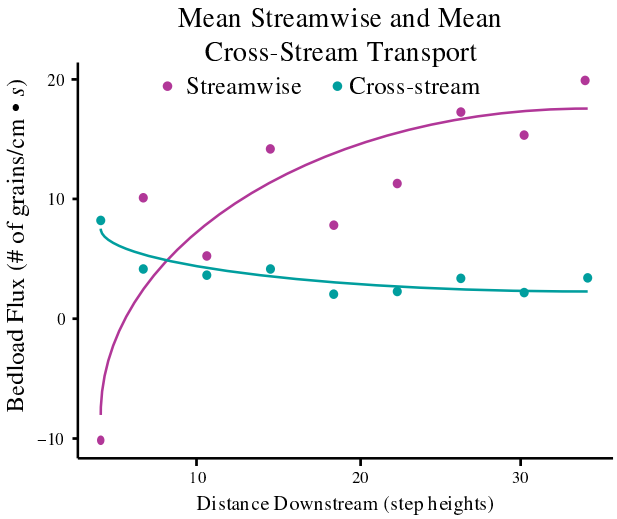

Figure 8. Mean streamwise and cross-stream bed load flux. Cross-stream transport shown above is the magnitude of both positive and negative cross-stream flux. Notably, mean streamwise and cross-stream flux are of similar magnitudes at distances proximal to flow reattachment. Negative streamwise bedload fluxes indicate transport in the upstream direction.

At 30.18 step heights, the primary sequence is an almost fully developed dominant, three-dimensional flow sequence: {−3 −2 2 1 4 −4} (Figure 7c and Table 7). At this distance downstream, the probability of this sequence stagnating in the horizontal direction between the −4 and 4 octants is still higher than the probability this sequence will move on in a cyclical manner from octant −4 to octant −3. However, the transition probabilities of {−4 +4} and {−4 −3} are very near even to one another at 0.369 and 0.361, respectively (Figure 7c and Table 7). This suggests that this primary sequence has almost fully developed into a cyclical, three-dimensional dominant flow sequence.

This more detailed analysis of fluid velocities at 6.56, 14.44, and 30.18 step heights is congruent with the Quantile-Quantile and percentile differencing analysis above. At 6.65 step heights, we see that the fluid velocity distributions in all three directions of flow have heavy tails. Additionally, it is around this distance that percentile differencing for negative vertical and positive streamwise fluid velocities peaks. Octant analysis in this region shows primary sequence fluctuations in the streamwise direction followed by a secondary sequence composed of fluid fluctuations down, into the bed. The magnitude of percentile differencing in this region suggests that these fluctuation sequences have larger magnitudes than similar fluctuations occurring downstream.

As we move farther downstream to 14.44 and 20.18 step heights, fluid velocity distributions (in all direction) become more normally distributed and therefore percentile differencing values are lower. This corresponds with the development of the {−3 2 2 1 4 −4} flow sequence. The magnitude of percentile differencing suggests that the fluid fluctuations in this region are smaller in magnitude than similar fluid fluctuations occurring upstream.

3.3. Bed Load Transport Patterns

3.3.1. Bed load Transport Time Series

The pattern of bed load transport also appears to change with distance downstream of flow reattachment. Bed load flux time series data show that near flow reattachment, cross-stream, and streamwise fluxes are of more similar magnitudes (Figures 8, 9a, and supporting information Figure S3). In contrast, far downstream of flow reattachment, the magnitude of average streamwise flux is about five times greater than the magnitude of average cross-stream flux. While mean streamwise flux increases nonlinearly, mean cross-stream flux decreases nonlinearly with increased distance from the backstep. This suggests a diminishing role in cross-stream transport at distances farther from the backstep.

3.3.2. Particle Tracking

Bed load flux time series data coupled with particle tracking data show distinct differences in the overall pattern of transport with increasing distance downstream of flow reattachment (Figure 9). It is clear from bed load flux time series plots (Figure 9a) that transport in both the streamwise and cross-stream directions is intermittent even at distances far away from flow reattachment (i.e., 30.18 step heights). However, periods of high-magnitude cross-stream flux are correlated with periods of high-magnitude streamwise flux at distances proximal and intermediate to flow reattachment (6.56 and 14.44 step heights). We do not see this same correlation of high-magnitude events at sampling locations distal to flow reattachment. Rather, at 30.18 step heights the magnitude of cross-stream transport events is much smaller than the magnitude of stream transport events.

This suggests that proximal to flow reattachment, transport events are intermittent and *multidirectional*. Distal to flow reattachment, transport events are still intermittent but largely unidirectional in the streamwise direction. Direction of transport data (Figure 9c) further supports the multidirectionality of transport near flow reattachment. At 6.56 step heights, we see that grains in transport move in a wide array of directions. The distribution of directions traveled by grains decreases with increasing distance downstream (Figure 9c).

Particle tracking videos suggest that not only is transport intermittent and multidirectional near flow reattachment, it is also localized. Supporting information Movies S1–S3 show the movement of sand grains during the large flux events highlighted in Figure 9a at 6.56, 14.44, and 30.18 step heights, respectively. At 6.56 step

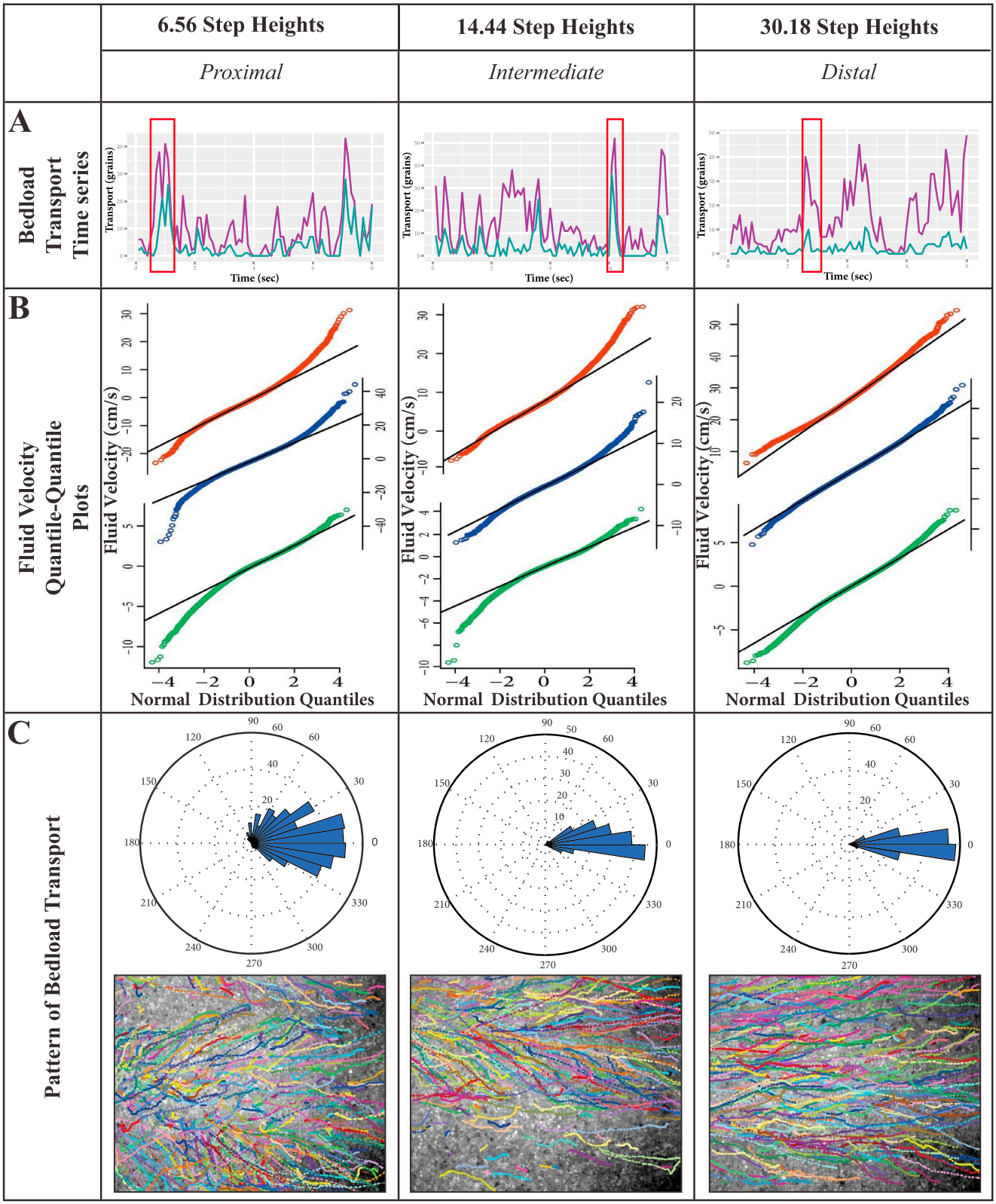

Figure 9. (a) Bed load transport (streamwise in purple and cross-stream in green) time series data for distances 6.56, 14.44, and 30.18 step heights downstream of the backstep. Red boxes indicate timing of transport events used for particle tracking analysis in Figure 9c. (b) Quantile-quantile plots of streamwise (u, red), cross-stream (v, blue), and vertical (w, green) fluid velocities. The solid black line represents where the data should plot if it were normally distributed. (c) Pattern of bed load transport particle tracking data and sample images. Rose diagrams show average direction each grain travels while in transport, where 0 indicates purely streamwise transport.

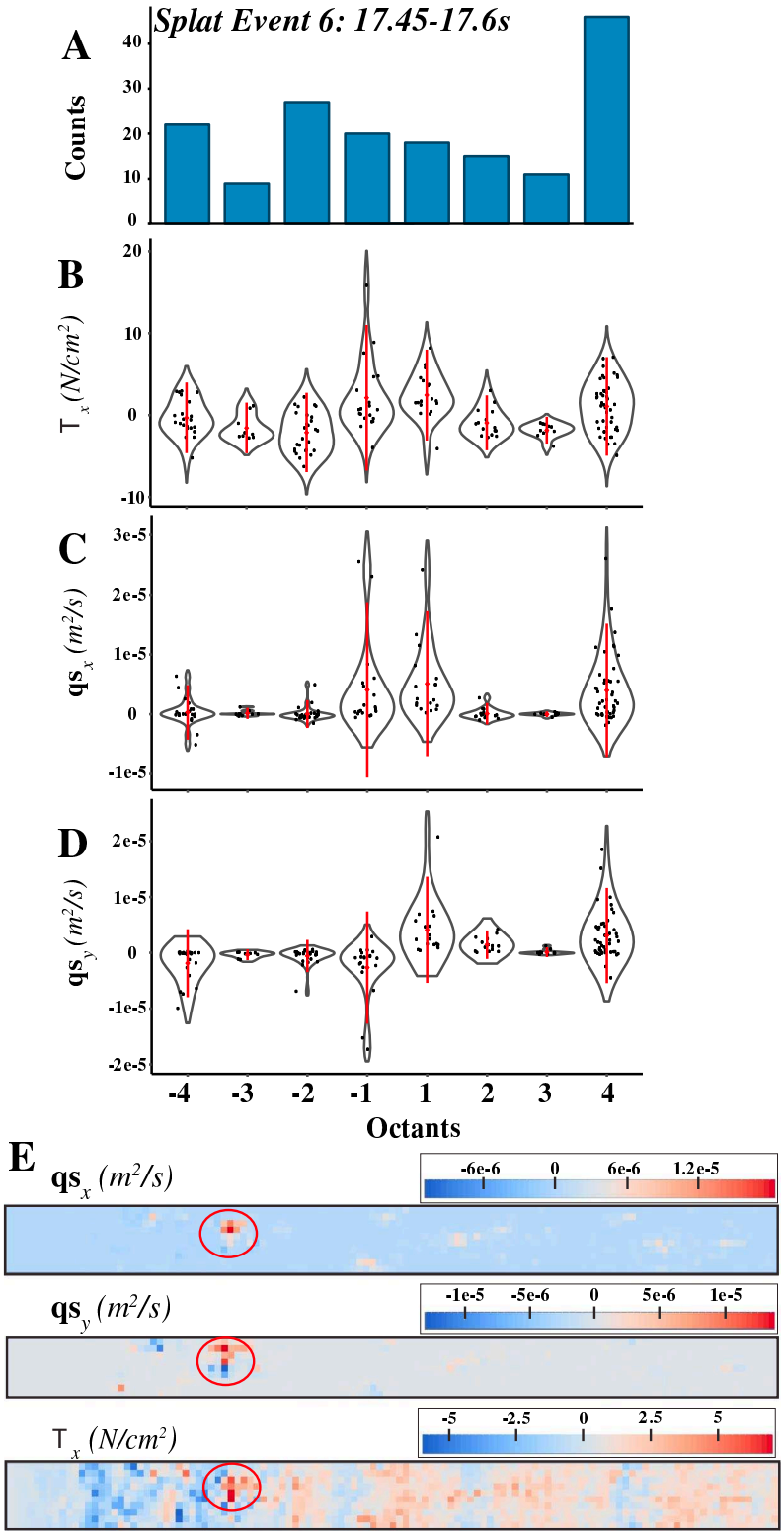

Figure 10. (a) Cumulative spatiotemporal octant, (b) near-bed shear stress, (c) streamwise transport, and (d) cross-stream transport for a (e) single-splat event. Red diamonds and bars in the violin plots of Figures 10b–10d are the mean and the extent of 2 standard deviations, respectively. Negative streamwise transport indicates transport in the upstream direction. Transport, both in the streamwise and cross-stream directions, corresponds primarily with −1, 1, −4, and 4 octants, which are the octant equivalent of outward interactions and sweep quadrant events. This is congruent with the secondary octant sequence identified in the ADV data at 6.56 step heights.

heights (supporting information Movie S1) particle tracking shows that the bulk of the sediment being transported through this event initiates in the bottom left-hand part of the field of view. At 14.44 step heights (supporting information Movie S2) transport is still fairly intermittent, as evidenced by the fact that barely any transport occurs in the lower half of the field of view. At 30.18 step heights (supporting information Movie S3), however, transport is initiated and occurring throughout the field view indicating that transport is no longer localized.

Combining bed load time series data with particle tracking videos shows that within the proximal to flow reattachment, transport is localized, intermittent, and multidirectional. Distal to flow reattachment, transport is dispersed throughout the field of view, intermittent, and unidirectional. The extent of localized, intermittent, and multidirectional transport also corresponds to heavier tailed velocity distributions (Figure 9b and supporting information Figure S4) and peak divergence from the mean in both streamwise and cross-stream velocities as indicated by percentile differencing (Figures 6b and 6c). Localized, intermittent, and multidirectional transport also spatially corresponds to where temporally intermittent octant sequences occur (Figure 7a).

3.4. Numerical Splat Analysis

The above analysis illustrates that bed load transport and fluid velocity patterns differ significantly near flow reattachment (i.e., 6.56 step heights) compared to farther downstream (14.44 and30.18 step heights). To connect patterns of bed load transport with fluid velocity patterns, we turn to numerical data from Schmeeckle (2015). In these numerical simulations, Schmeeckle (2015) noted the presence and importance of splat events in the region just downstream of flow reattachment. We explore these numerical splat events in more detail for two reasons: (1) The region in which these events are dominant described in Schmeeckle (2015) is similar to the region in which we see distinctly different bed load transport and fluid velocity patterns in our flume experiments and (2) The pattern of bed load transport (i.e., localized, intermittent, and multidirectional) observed in our bed load tracking analysis is congruent with the bed load transport patterns associated splat events, as described by previous investigations (Schmeeckle, 2015; Stoesser et al., 2008; Perot & Moin, 1995).

Detailed analysis of splat events in the numerical simulations of Schmeeckle (2015) is presented in Figure 10 and supporting information Figures S5 and S6. The single-splat event shown in Figure 10 highlights that although the fluid flow during a splat event does generally include all octants (Figure 10a) transport (in both the cross-stream and downstream directions) is primarily associated with −1, 1, 4, and −4 octants (Figures 10c and 10d). Further, supporting infomration Figures S6 and S7 show that all six splat events analyzed show peaks in streamwise and cross-stream transport during −1, 1, 4, and −4 octant events. Additionally, high near-bed shear stress is often, but not always, associated with −1, 1, 4, and −4 octant events (Figure 10b and supporting information Figures S6 and S7).

4. Discussion

Results reported here are in agreement with results presented by Nelson et al. (1995) and Schmeeckle (2015). As noted by Nelson et al. (1995), near-bed shear stress cannot accurately account for the increase in bed load transport downstream of flow reattachment. We report similar findings here but did not identify a peak in transport ∼20 step heights downstream of the backstep as Nelson et al. (1995) did. Rather, we report a nonlinear increase of bed load transport with increasing distance downstream. Octant analysis conducted herein is in agreement with the quadrant analysis completed by Nelson et al. (1995) in that we see outward interactions (Quadrant 1; Octants −1 and 1) and sweep events (Quadrant 4; Octants −4 and 4) playing a key role in transport, particularly near flow reattachment. Schmeeckle (2015) reported similar findings to this effect.

As previously mentioned, Schmeeckle (2015) also noted the presence and importance of splat events. In the numerical simulations of Schmeeckle (2015), splat events manifested within larger sweep structures of the flow and were prevalent closest to the backstep and diminished in frequency and size with increasing distance from the backstep. The numerical experiments exhibited low-frequency fluid pressure fluctuations, wherein high pressure was associated with high-transport splat events and sweeps and outward interactions (i.e., quadrants 4 and 1 events). Whereas, low-pressure fluctuations where associated with low transport and bursts and inward interactions (i.e., quadrants 2 and 3 events). Although fluid pressure and vertical fluid velocity was not measured simultaneously with sediment movement in the present study, the radiating pattern of transport from intermittent events near flow reattachment (see Figure 9c and supporting information Movie S1) is consistent with numerical results of Schmeeckle (2015).

Additionally, new analyses investigating the dynamics of splat events from the numerical simulations reported herein indicate further that the transport initiated during a splat event is primarily associated with outward interactions and sweep events (i.e., octants −1, 1, 4, and −4). These same octants form a secondary flow sequence at 6.56 step heights (i.e., the region in which we see transport patterns similar to those of splat events). Given this new analysis, in conjunction with data presented in Schmeeckle (2015) and the previously documented assertion that splat events are the combination of a sweep and an outward interaction, we suggest that the secondary sequence observed at 6.56 step heights, {1 4 −4} is the octant sequence responsible for splat events (Figure 3). This sequence of octants paired with the distinct pattern of localized, intermittent, multidirectional bed load transport at 6.56 step heights indicates a high possibility that splat events are the primary mechanism responsible for bed load transport in the region just downstream of flow reattachment in the flume experiments presented herein. Octant sequence probabilities and pattern of bed load transport results reported here indicate that this zone does not extend past 14.44 step heights.

The existence of splat events and their importance to the initiation and pattern of bed load transport near flow reattachment cannot be neglected from future modeling that focuses on bed load transport over bed forms on the bed form scale. By looking at the sub–bed form scale, we see that not only are splat events important to initiating the movement of sediment near flow reattachment, they heavily influence where sediment goes. As indicated by bed load transport pattern data reported here, near flow reattachment bed load transport has a large cross-stream component. This is significant when considering the evolution of bed forms through time.

Cross-stream transport has been assumed to be a secondary, diffusive process, depending linearly on cross-stream bed slope (Jerolmack & Mohrig, 2005; Murray & Paola, 1997). Results reported here, however, prompt the question: is the lateral movement of bed load only a diffusive process dependent on slope? Each splat event causes considerable cross-stream transport. In the case of these backward facing step experiments, net cross-stream transport is most likely zero due to the back and forth motion of multiple events. However, this is a product of a straight, undeforming backward facing step upstream. In the case of complex, evolving, three-dimensional bed forms, however, the flow field changes depending on the geometry of the upstream form (Venditti, 2007). In such circumstances, it seems reasonable to assume that the number and intensity of splat events will vary laterally, leading to net lateral transport from a gradient in grain transport activity (Furbish et al., 2012). It is also probable that splat events are asymmetric in their net transport when the bed form crestline varies in position and height in the cross-stream direction. In order to better model and understand bed load transport over and evolution of bed forms, splat events and their role in initiating entrainment needs to be accounted for.

5. Conclusion

Flume experiments modeled after Nelson et al. (1995) assess the affects of flow separation and reattachment due to a backward facing step on downstream turbulent structures and bed load transport. Fluid velocities were analyzed qualitatively using PIV and Quantile-Quantile plots and quantitatively using percentile differencing techniques. Fluid velocity patterns were assessed using octant analysis and Markovian transition probabilities. Bed load transport patterns were assessed using time series analysis and manual particle tracking techniques. Splat events from numerical simulations (Schmeeckle, 2015) were analyzed to assess the role of different fluid velocity fluctuations to splat event dynamics. These numerical results were then compared to experimental fluid velocity fluctuation and bed load transport pattern data to assess the potential role of splat events in real (i.e., nonnumeric) situations. Results reported here show that

1. Flow separation/reattachment and associated downstream turbulent structures play a significant role in the pattern of transport downstream.
2. Traditional bed load transport equations underestimate observed bed load transport at all distances downstream of the backward facing step.
3. Fluid velocity distributions also differ at distances proximal, intermediate, and distal to flow reattachment. Proximal to flow reattachment, we see large-magnitude streamwise velocity events, relative to the mean streamwise velocity. Additionally, there is an increase in large-magnitude negative vertical velocity events (irrespective of the mean).
4. Octant analysis at 6.56, 14.44, and 30.18 step heights show distinct differences of flow patterns. Proximal to flow reattachment (6.56 step heights), flow is composed of segmented primary, secondary, and tertiary fluid sequences. At intermediate distances from flow reattachment (14.44 step heights), we see the development

of a dominant, three-dimensional flow sequence: {−3 −2 2 1 4 −4}. This sequence becomes fully formed at locations distal to flow reattachment (30.18 step heights and greater).

5. Distances proximal to flow reattachment show distinct differences in bed load transport pattern compared to sampling locations farther downstream. While streamwise bed load transport increases nonlinearly with distance downstream, cross-stream transport decreases nonlinearly. Bed load transport proximal to flow reattachment consists of intermittent, localized, multidirectional transport events that move sediment comparable magnitudes in both the streamwise and cross-stream directions. Distal to flow reattachment, transport events move sediment primarily in the streamwise direction.
6. Analysis of numerical splat events (Schmeeckle, 2015), coupled with patterns of bed load transport and octant analysis data, strongly suggests the flow sequence {1 4 −4} is associated with splat events.
7. Bed load transport pattern and fluid velocity fluctuation data are both consistent with the existence of permeable splat events. Splat events play a large role in bed load transport close to flow reattachment and should be considered in future models of bed load transport over bed forms. Additionally, splat events should be explored in more detail to investigate their potential role in bed form evolution.

Acknowledgments
This research was supported by a National Science Foundation research grants (award: 1226288 and 1734752) awarded to Mark Schmeeckle. I am very thankful to the three anonymous JGR reviewers, the anonymous Associate Editor, and especially John Buffington for their thoughtful and constructive reviews. All data presented in this article can be found at https://doi.org/10.5967/M0TB150B.

References

Allen, J. (1966). On bed forms and paleocurrents. *Sedimentology*, *6*(3), 153–190.
Bagnold, R. A. (1941). *The physics of wind blown sand and desert dunes*. London, England: Methuen.
Bennett, S. J., & Best, J. L. (1995). Mean flow and turbulence structure over fixed, two-dimensional dunes: Implications for sediment transport and bedform stability. *Sedimentology*, *42*, 491–513. https://doi.org/10.1111/j. 1365-3091.1995.tb00386.X
Best, J. L. (2005). The fluid dynamics of river dunes: A review and some future research directions. *Journal of Geophysical Research*, *110*, F04S02. https://doi.org/10.1029/2004JF000218
Carling, P. A. (1999). Subaqueous gravel dunes. *Journal of Sediment Research*, *69*(3), 534–545. https://doi.org/10.2110/jsr.69.534
Carling, P. A. (2005). A flume experiment on the development of subaqueous fine-gravel dunes from a lower-stage plane bed. *Journal of Geophysical Research*, *110*, F04S05. https://doi.org/10.1029/2004JF000205
Dinehart, R. L. (1992). Evolution of coarse gravel bed forms: Field measurements at flood stage. *Water Resources Research*, *28*(10), 2667–2689.
Duan, J. G. (2004). Discussion of "Simulation of flow and mass dispersion in meandering channels". *Journal of Hydraulic Engineering*, *130*(10), 964–976. https://doi.org/10.1061/ASCE0733-94292004130:10964
Emadzadeh, A., & Cheng, N.-S. (2016). Measurements of sediment pickup rate over dune-covered bed. *Environmental Fluid Mechanic*, *16*, 123–144. https://doi.org/10.1007/s10652-015-9416-1
Engel, P. (1981). Length of flow separation over dunes. *Journal of the Hydraulics Division*, *107*(10), 1133–1143.
Finn, J. R., Li, M., & Apte, S. V. (2016). Particle based modeling and simulation of natural sand dynamics in the wave bottom boundary layer. *Journal of Fluid Mechanics*, *796*, 340–385.
Furbish, D. J., Haff, P. K., Roseberry, J. C., & Schmeeckle, M. W. (2012). A probabilistic description of the bed load sediment flux: 1. Theory. *Journal of Geophysical Research*, *117*, F03031. https://doi.org/10.1029/2012JF002352
Grinstead, C. M., & Snell, J. L. (2012). *Introduction to probability*. Providence, Rhode Island: American Mathematical Society.
Jerolmack, D. J., & Mohrig, D. (2005). A unified model for subaqueous bed form dynamics. *Water Resources Research*, *41*, W12421. https://doi.org/10.1029/2005WR004329
Jovic, S., & Driver, D. M. (1994). Backward-facing step measurements at low Reynolds number, Re (sub h) = 5000 (*NASA Technical Memorandum*). Moffett Field, CA: Ames Research Center.
Keylock, C. J., Lane, S. N., & Richards, K. S. (2014). Quadrant/octant sequencing and the role of coherent structures in bed load sediment entrainment. *Journal of Geophysical Research: Earth Surface*, *119*, 264–286. https://doi.org/10.1002/2012JF002698
Kidanemariam, A. G., & Uhlmann, M. (2014a). Direct numerical simulation of pattern formation in subaqueous sediment. *Journal of Fluid Mechanics*, *750*, R2.
Kidanemariam, A. G., & Uhlmann, M. (2014b). Interface-resolved direct numerical simulation of the erosion of a sediment bed sheared by laminar channel flow. *International Journal of Multiphase Flow*, *67*, 174–188.
Kleinhans, M. G. (2001). The key role of fluvial dunes in transport and deposition of sand-gravel mixtures, a preliminary note. *Sedimentary Geology*, *143*(1–2), 7–13. https://doi.org/10.1016/S0037-0738(01)00109-9
Kleinhans, M. G., Wilbers, A. W. E., De Swaaf, A., & Van Den Berg, J. H. (2002). Sediment supply-limited bedforms in sand-gravel bed rivers. *International Journal of Sediment Research*, *72*(5), 629–640.
Kwoll, E., Venditti, J. G., Bradley, R. W., & Winter, C. (2016). Flow structure and resistance over subaquaeous high- and low- angle dunes. *Journal of Geophysical Research: Earth Surface*, *121*, 545–564. https://doi.org/10.1002/2015JF003637
Le, H., Moin, P., & Kim, J. (1997). Direct numerical simulations of turbulent flow over a backward-facing step. *Journal of Fluid Mechanics*, *330*, 349–374. https://doi.org/10.1017/S0022112096003941
Madden, M. M. (1997). Octant analysis of the Reynolds stresses in the three dimensional turbulent boundary layer of a prolate spheroid (MSc thesis). VA: Aerospace Engineering, Virginia Polytechnic Institute Blacksburg.
Meyer-Peter, E., & Müller, R. (1948). Formulas for bed-load transport. In *Proceedings 2nd Meeting, IAHR* (pp. 39–64). Stockholm, Sweden.
McElroy, B., & Mohrig, D. (2009). Nature of deformation of sandy bed forms. *Journal of Geophysical Research*, *114*, F00A04. https://doi.org/10.1029/2008JF001220
McLean, S. R., Nelson, J. M., & Wolfe, S. R. (1994). Turbulence structure over two-dimensional bed forms: Implications for sediment transport. *Journal of Geophysical Research*, *99*(C6), 12,729–12,747. https://doi.org/10.1029/94JC00571
McLean, S. R., Wolfe, S. R., & Nelson, J. M. (1999a). Predicting boundary shear stress and sediment transport over bed forms. *Journal of Hydraulic Engineering*, *125*(7), 725–736. https://doi.org/10.1061/(ASCE)0733-9429(1999)125:7(725)
McLean, S. R., Wolfe, S. R., & Nelson, J. M. (1999b). Spatially averaged flow over a wavy boundary revisited. *Journal of Geophysical Research*, *10*, 15,743–15,753.
Meijering, E., Dzyubachyk, O., & Smal, I. (2012). Methods for cell and particle tracking. *Methods in Enzymology*, *504*(9), 183–200.

Murray, A. B., & Paola, C. (1997). Properties of a cellular braided-stream model. *Earth Surface Processes and Landforms*, *22*(11), 1001–1025. https://doi.org/10.1002/(SICI)1096-9837(199711)22:11<1001::AID-ESP798>3.0.CO;2-O

Nelson, J. M., McLean, S. R., & Wolfe, S. R. (1993). Mean flow and turbulence fields over two-dimensional bed forms. *Water Resources Research*, *29*(12), 3935–3953.

Nelson, J. M., Shreve, R. L., McLean, S. R., & Drake, T. G. (1995). Role of near-bed turbulence structure in bed load transport and bed form mechanics. *Water Resources Research*, *31*(8), 2071–2086. https://doi.org/10.1029/95WR00976

Nikuradse, J. (1933). Stromungsgesetze in rauhen Rohren. In *Forschung auf dem Gebiete des Ingenieurwesens*. Berlin, Germany: Forschungsheft 361 VDI Verlag.

Perot, B., & Moin, P. (1995). Shear-free turbulent boundary layers. Part 1. Physical insights into near- wall turbulence. *Journal of Fluid Mechanics*, *295*, 199–227.

Roseberry, J. C., Schmeeckle, M. W., & Furbish, D. J. (2012). A probabilistic description of the bed load sediment flux: 2. Particle activity and motions. *Journal of Geophysical Research*, *117*, F03032. https://doi.org/10.1029/2012JF002353

Rubin, D. M. (2012). A unifying model for planform straightness of ripples and dunes in air and water. *Earth Science Reviews*, *113*(3–4), 176–185. https://doi.org/10.1016/j.earscirev.2012.03.010

Schmeeckle, M. W. (2014). Numerical simulation of turbulence and sediment transport of medium sand. *Journal of Geophysical Research: Solid Earth*, *119*, 1240–1262. https://doi.org/10.1002/2013JF002911

Schmeeckle, M. W. (2015). The role of velocity, pressure, and bed stress fluctuations in bed load transport over bed forms: Numerical simulation downstream of a backward-facing step. *Earth Surface Dynamics Discuss*, *2*(2), 715–732. https://doi.org/10.5194/esurfd-2-715-2014

Schmeeckle, M. W., Nelson, J. M., & Shreve, R. L. (2007). Forces on stationary particles in near-bed turbulent flows. *Journal of Geophysical Research*, *112*, F02003. https://doi.org/10.1029/2006JF000536

Shields, A. (1936). Anwendung der Aechlichkeitsmechanik und der Turbulenz Forschung auf die Geschiebebewegung. In *Mitteilungen der Pruessischen Versuchsanstalt fuer Wasserbau and Schiffbau* (Vol. 26, pp. 1–26). Berlin, Germany.

Smith, J. D., & McLean, S. R. (1977). Spatially averaged flow over a wavy surface. *Journal of Geophysical Research*, *82*(12), 1735–1746.

Stoesser, T., Braun, C., Garcia-Villalba, M., & Rodi, W. (2008). Turbulence structures in flow over two-dimensional dunes. *Journal of Hydraulic Engineering*, *134*(1), 42–55.

Sumer, B. M., Chua, L. H. C., Cheng, N.-S., & Fredsøe, J. (2003). Influence of turbulence on bed load sediment transport. *Journal of Hydraulic Engineering*, *129*(8), 585–596. https://doi.org/10.1061/(ASCE)0733-9429(2003)129:8(585)

Sun, R., Xiao, H., & Strom, K. (2016). Particle dynamics in self-generated dunes over a range of hydraulic and sediment transport conditions using LES–DEM. *arXiv preprint arXiv*, *1610. 03397*.

Venditti, J. G. (2007). Turbulent flow and drag over fixed two- and three-dimensional dunes. *Journal of Geophysical Research*, *112*, F04008. https://doi.org/10.1029/2006JF000650

Venditti, J. G., Church, M., & Bennett, S. J. (2005). On the transition between 2D and 3D dunes. *Sedimentology*, *52*(6), 1343–1359. https://doi.org/10.1111/j.1365-3091.2005.00748.X

Wong, M., & Parker, G. (2006). Reanalysis and correction of bed-load relation of Meyer-Peter and Müller using their own database. *Journal of Hydraulic Engineering*, *132*(11), 1159–1168. https://doi.org/10.1061/(ASCE)0733-9429(2006)132:11(1159)